Open Ceramics 14 (2023) 100348

Contents lists available at ScienceDirect

Open Ceramics

journal homepage: www.sciencedirect.com/journal/open-ceramics

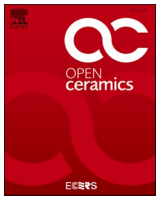

# Additive manufacturing of calcium carbonate parts through vat-photopolymerization and sintering in carbon dioxide atmosphere

Mateus Mota Morais [a,b,*], Italo Leite de Camargo [a,c], Paolo Colombo [b,d], Carlos Alberto Fortulan [a]

[a] Department of Mechanical Engineering, São Carlos School of Engineering, University of São Paulo, Trabalhador São-carlense, 400, São Carlos, SP, 13566-590, Brazil
[b] Department of Industrial Engineering, University of Padova, 35131, Padova, Italy
[c] Federal Institute of Education, Science and Technology of São Paulo, IFSP, Primeiro de Maio, 500, Itaquaquecetuba, SP, Brazil
[d] Department of Materials Science and Engineering, The Pennsylvania State University, University Park, PA, 16802, United States

ARTICLE INFO

*Keywords:*
Calcium carbonate
Calcite
Vat-photopolymerization
DLP
3D printing
Sintering

ABSTRACT

Although calcium carbonate is more commonly used in powder form, it could have exciting applications in bulk form, such as bone scaffolds, synthetic corals, and artificial rocks. Additive manufacturing (vat-photopolymerization) is a promising strategy for producing parts with complex geometries. However, two main challenges arise: 1) Producing a $CaCO_3$ suspension with high solid loading and low viscosity suitable to ordinary bottom-up 3D printers; 2) Debinding and sintering the $CaCO_3$ parts without causing their thermal decomposition. The first challenge was addressed by following a systematic methodology to select the monomer and dispersant, resulting in a printable 35 vol% $CaCO_3$ suspension with low viscosity (0.28 Pa s at $30s^{-1}$). The second challenge was overcome by debinding in air atmosphere to remove all organics, followed by sintering in $CO_2$ above 500 °C to avoid the calcination of $CaCO_3$. The presented results are an important advance for the fabrication of calcium carbonate parts with complex geometries.

## 1. Introduction

Calcium carbonate ($CaCO_3$) powder is an essential feedstock material used in several sectors, such as construction, agriculture, and pharmacy [1,2]. It is also commonly used in ceramic processing as a pore former [3]. Although $CaCO_3$ is mostly used in powder form, bulk and structural parts of this material could have interesting applications. For instance, calcium carbonate with hierarchical porosity is a promising bone scaffold material [4–7] due to its good biocompatibility, fast absorption, good cell adhesion, and lower price compared to other potential bioceramics [6–11]. It could also be used for coral reef restoration [12] because it is similar to the material found in natural corals [13].

Another important possible application is creating models of carbonate rocks for petroleum engineering and geophysics studies [14,15]. However, the natural carbonate rocks found in petroleum fields have a high cost of extraction, are limited in number and very heterogeneous (even from samples drilled from the same region) [15–17]. Consequently, it is challenging to obtain reproducible and comparable results using them, especially when destructive tests are involved (such as compressive tests, mercury injection porosimetry, and acid injection) [17–20]. As a possible solution, it has been proposed to fabricate artificial rocks [14–16,21–29] and microfluidic models [29–32] with controllable and reproducible features, tuning the petrophysical properties and reducing the experimental error obtained when testing natural rocks. Such artificial rock models would be an essential tool for developing and validating numerical models and simulations, obtaining experimental correlations between the microstructure and the petrophysical properties (including permeability, mechanical and acoustic properties) [14,21,26], and studying enhanced oil recovery (EOR) technics [27,28,33–36].

However, producing calcium carbonate parts is not straightforward. There are two main challenges. The first is sintering the $CaCO_3$ without causing its thermal decomposition into CaO and $CO_2$. Its calcination

*Abbreviations:* DLP, Digital Light Processing; HEMA, 2-Hydroxyethyl methacrylate; PEGDA, Poly(ethylene glycol) diacrylate; SEM, Scanning Electron Microscopy; TGA, Thermogravimetric analysis; XRD, X-ray diffraction.

* Corresponding author. Department of Mechanical Engineering, São Carlos School of Engineering, University of São Paulo, Trabalhador São-carlense, 400, São Carlos, 13566-590, Brazil.
*E-mail addresses:* mateus.morais@usp.br (M.M. Morais), italo.camargo@ifsp.edu.br (I.L. Camargo), paolo.colombo@unipd.it (P. Colombo), fortulan@usp.br (C.A. Fortulan).

https://doi.org/10.1016/j.oceram.2023.100348
Received 30 December 2022; Received in revised form 21 February 2023; Accepted 22 March 2023
Available online 25 March 2023

starts above 500 °C in air atmosphere [37–40], below the temperature required for its sintering (>800 °C), which is necessary to promote the coalescence of the particles, to reduce the porosity, and to increase the mechanical strength of the part [41,42]. As a possible solution, it is known that increasing the partial pressure of $CO_2$ inhibits the decarbonation of $CaCO_3$ and increases its decomposition temperature [38]. Using this idea, some researchers were able to sinter $CaCO_3$ at temperatures around 850–900 °C [8,11,43]. The same strategy was followed in a prior study from our research group [1], in which calcite was sintered in a carbon dioxide atmosphere at 850 °C, resulting in bulk calcium carbonate parts with high relative density (88%) and compressive strength of 110 MPa, similar to what is found in natural carbonates rocks (35–120 MPa) [44].

The second challenge is fabricating the complex geometries of corals, artificial rocks, and bone scaffolds, especially considering that the last two can possess a multiscale porosity [45–47]. Many authors have reported producing porous calcium carbonate samples through powder compaction. In their studies, the porosity was controlled either by adjusting the particle size distribution [15,25], the amount of binder or cement [16,25,28], or by adding a sacrificial pore former that is later removed thermally or by dissolution [5,11,27,48]. (Tables S1 and S2 in the Supplementary Material present an overview of the different strategies and materials used to fabricate artificial rocks using these conventional ceramic manufacturing routes). However, these approaches have limited control over the pore size and shape and cannot reliably replicate the same pore structure in different samples.

On the other hand, additive manufacturing is a promising strategy for producing complex geometries with designed porosity [49,50]. Another great advantage is the possibility of replicating geometries obtained directly from natural samples (such as a bone or a porous rock) through microtomography or 3D scanning [12,14,20,51]. Different 3D printing technologies have been proposed to produce artificial rocks, including Material Extrusion [52–57], Binder Jetting [17–19,51,57–71], Material Jetting [52,72–79] Vat-Photopolymerization [20,57,71,73,76,78,80] (and its high-resolution version, Two-Photon Polymerization [81–83]). In the Supplementary Material, Table S3 presents an extended list of references concerning artificial rocks produced by different additive manufacturing technologies with the pros and cons of each method.

After comparing these additive manufacturing technologies, some authors claim that vat-photopolymerization is the most recommended one to produce artificial porous rocks [71,84,85]. The main reason is its excellent resolution (≈25–100 μm for external features [86–91] and ≈300–400 μm for inner pores and channels [92,93]), which surpasses most other techniques [21]. Moreover, concerning ceramic materials, it is able to achieve good mechanical properties (for instance, 554 and 741 MPa of flexural strength for alumina and zirconia, respectively) [87,91,94–99] and densification higher than 99% [86,91]. There are three main categories of vat-photopolymerization depending on the light source: a) point-wise vector scanning of the light source (usually a laser) such as in stereolithography (SLA) [86,100]; b) mask projection by irradiating the entire layer at once (layer-wise) using an LCD screen or a light projector (Digital Light Processing (DLP)) [86,100] and c) two-photon polymerization, which is a point-wise approach that cures the material at the intersection of two laser beans, it has an outstanding high-resolution (up to 10 nm) but is currently limited to small sized samples (usually smaller than 1 mm) [81–83,100]. Furthermore, the vat-photopolymerization printers can also be classified according to the building direction. In the "bottom-up" approach, the light source is projected under the vat, and the build platform moves upwards as the new layers are formed (the part is printed upside-down), while in the "top-down" approach, the light source is projected from above and the build platform moves downwards as new layers are formed [88] (See Fig. 1).

However, vat-photopolymerization also has its drawbacks. First, producing a ceramic suspension suitable for vat-photopolymerization with high solid loading (≥40 vol%) and low viscosity (<3 Pa s) is a great challenge [87,101–103]. The low viscosity requirement is even more critical when using lower-cost bottom-up 3D printers that do not employ the complex recoating mechanisms present in the more advanced machines dedicated to ceramic materials [87,97,102,103]. Additionally, there is a limited selection of ceramic photocurable suspensions commercially available [104], and calcium carbonate is not one of them. In fact, most attempts to produce artificial rocks through additive manufacturing have used materials with a chemical composition different from calcium carbonate, such as polymers (for material extrusion [52,53,57], material jetting [73,76,79], and vat-photopolymerization [20,71,80]), gypsum [51,59,68,71] and silica sand [62,64,71] (for binder jetting). Nevertheless, a few researchers were able to 3D print calcium carbonate by preparing their own formulations for material extrusion [12,105,106] and vat-photopolymerization [6].

Furthermore, there are also drawbacks related to the debinding stage, which is one of the most critical steps in the production of ceramics through vat-photopolymerization [91]. During debinding, all the organics (polymers and additives) should be removed by oxidation or pyrolysis, leaving behind only the ceramic matrix [91]. The process should be carried out at slow and controlled heating rates (commonly <1 °C/min) to avoid cracking the fragile ceramic matrix that has not

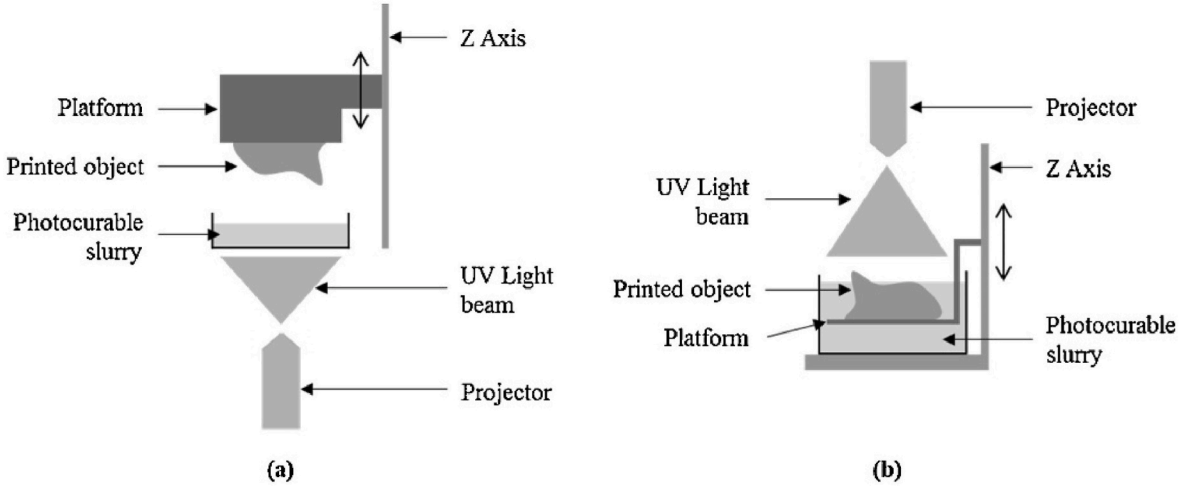


**Fig. 1.** Comparison between the two operating principles of vat-photopolymerization 3D printers: (a) bottom-up; (b) top-down. Obtained from Ref. [88] with permission from Elsevier.

been sintered yet [42,91,107]. This challenge is especially tricky for calcium carbonate compared to other ceramics. On one side, $CaCO_3$ is sintered at a relatively low temperature (≈850–900 °C) compared to other ceramic materials, which makes it difficult to completely remove the organics through pyrolysis. On the other side, $CaCO_3$ sintering requires a $CO_2$ atmosphere above 500 °C, making it difficult to remove the organics through oxidation. Therefore, the recommended sintering atmosphere is not suitable for the oxidation of the organics while the sintering temperature is too low for their pyrolysis. Because of this challenge, the attempts to print calcium carbonate through photopolymerization did not employ any heat treatment [12] or, in the best case, carried out only the debinding up to 500 °C, without sintering the material [6].

This paper describes a systematic approach to produce a photocurable calcium carbonate suspension with very low viscosity (<0.5 Pa s at 30 $s^{-1}$) that could be successfully used in an ordinary bottom-up vat-photopolymerization 3D printer. Moreover, it describes how to set up the heat treatment to remove all the organics during debinding in air atmosphere, followed by sintering the $CaCO_3$ without thermal decomposition using a $CO_2$ atmosphere. The combination of these approaches resulted in sintered parts totally constituted of calcium carbonate.

## 2. Materials and methods

### 2.1. Materials

The ceramic powder used was a high-purity $CaCO_3$ powder (Lab-Synth, Brazil) with a calcite crystalline structure (confirmed by X-Ray diffraction, Shimadzu XRD-7000 Maxima X). The true density of the powder was 2.7005 g/$cm^3$ (Pycnometer Quantachrome Ultrapyc 1200e, 10 purges), and the BET surface area was 10.73 $m^2$/g (Quantachrome - Nova Station 1200e). The powder had a median agglomerate diameter ($d_{50}$) of about 1.567 μm (measured by X-Ray monitored sedimentation, Micromeritics SediGraph III Plus), while $d_{90}$ and $d_{10}$ were 3.03 μm and 0.475 μm, respectively. The size distribution can be found in Fig. S1 in the Supplementary Material. The agglomerates were composed of needle-like particles of calcite, with the longer axis measuring around 1 μm or smaller and an aspect ratio of about 1:4, as observed through Scanning Electron Microscopy (SEM, FEI Helios NanoLab 600i, with an accelerating voltage of 2 kV and current of 11 pA), see Fig. 2. The small particle size and its rough surface explain the relatively large surface area of the powder.

The candidate monomers were 2-Hydroxyethyl methacrylate (HEMA) and poly(ethylene glycol) diacrylate with an average molecular weight of 250 g/mol (PEGDA 250), both bought from Sigma-Aldrich. The 8 candidate dispersants were oleic acid (LabSynth, Brazil), Ammonium polyacrylate, Triton X-100 (polyethylene glycol tert-octylphenyl ether, a non-ionic surfactant with hydrophilic polyethylene chain and an aromatic hydrophobic group obtained from Sigma Aldrich), BYK-w966 and BYK-w 980 (both are a solution of a salt of unsaturated polyamine amides and acidic polyesters, from BYK), BYK-w 985 (a solution of an acidic polyester, from BYK), Solsperse 41000 (a polymeric alkoxylate, from Lubrizol) and Solsperse 85000 (a phosphodiester polymeric dispersant, from Lubrizol). The dispersants were pre-selected, considering the desired compatibility between the calcium carbonate surface and the medium (monomer). Finally, the photoinitiator employed was phenylbis(2,4,6-trimethyl benzoyl)phosphine oxide (Sigma Aldrich).

### 2.2. Formulation of the ceramic suspension

The first challenge was preparing a calcium carbonate suspension with moderate to high solid loading (35–55 vol%) [87,101] while maintaining a viscosity lower than 0.5 Pa s at 30 $s^{-1}$ to be suitable for ordinary polymer DLP printers. The proposed methodology followed 3 steps: 1) Selecting the appropriate monomer composition considering the viscosity and reactivity (cured thickness); 2) Selecting the dispersant with the best viscosity reduction; 3) Increasing the ceramic solid loading without surpassing the viscosity limit. The viscosity was evaluated at a shear rate of 30 $s^{-1}$, which is commonly used as a reference for the vat-photopolymerization process [101,103,108].

#### 2.2.1. Selection of the monomer

In the first stage, the main monomer considered was the diacrylate PEGDA 250 because of the successful previous experiences of our research group [109–112]. Elsayed et al. [4] also obtained good results with calcium carbonate using a similar monomer. Aiming at reducing the viscosity, HEMA, a monofunctional methacrylate with low viscosity, was considered as a potential reactive diluent [87]. The following compositions were prepared by mixing PEGDA 250 with increasing contents of HEMA: 0% (pure PEGDA), 5%, 10%, 33%, 67%, and 100% (pure HEMA). Each formulation included 15 vol% of calcium carbonate powder, and the materials were mixed for 24 h in a roller ball mill.

The viscosity of each composition was analyzed at room temperature (21–23 °C) using a rotational viscometer (Brookfield DVT2 LV) with a coaxial cylinder geometry sample (using the sample chamber SC4-13R and the spindle SC4-34). The average steady-state torque was measured at the following shear rates 1, 5, 10, 20, 30, 40, and 50 $s^{-1}$. Then, 2 wt% (in relation to the monomers) of photoinitiator was added to the suspension and mixed for additional 16 h. Finally, the cured thickness of each composition was measured for an exposure time of 1, 2, 5, 10, 20, and 50 s using the light projector of the Creality LD-002H DLP 3D printer (irradiance energy of 8 mW/$cm^2$ and light wavelength of 405 nm).

#### 2.2.2. Selection of the dispersant

The second stage was the selection of the best dispersant among the 8 pre-selected ones. The dispersant amount was fixed at 2 wt% (in relation to the ceramic powder) based on the supplier's recommendation of 2 mg/$m^2$ of dispersant per surface area of the powder. Then, 8 samples, each containing one of the proposed dispersants, were manually mixed with PEGDA. Then, 15 vol% of $CaCO_3$ powder was added to each

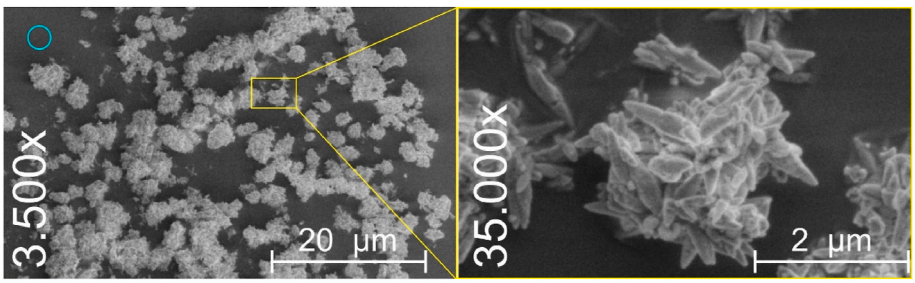


**Fig. 2.** SEM images of the calcium carbonate powder used in this study. The blue circle in the upper left corner represents the diameter of the median agglomerate measured with X-ray monitored sedimentation. On the right is the magnification of one agglomerate evidencing the needle-like particles of calcite. (For interpretation of the references to colour in this figure legend, the reader is referred to the Web version of this article.)

sample, and the suspensions were mixed for 24 h in the roller ball mill. The viscosity of each composition was measured with the rotational viscometer, as described in the previous section. The appropriate spindle diameter for each suspension was chosen among the available models (SC4-18, SC-31, SC4-34, and SC4-25) based on their measurable viscosity range (smaller diameters (larger gap) for more viscous suspensions).

#### 2.2.3. Increasing the solid loading

Finally, after choosing the best monomer (PEGDA) and the best dispersant (Solsperse 85000), formulations with an increasing amount of calcium carbonate were prepared (30, 35, 40, 45, and 50 vol%). The suspensions were mixed in a vibratory ball mill until homogenization (12 h for the samples with 30, 35, and 40 vol%; and 24 h for the ones with 45 and 50 vol%). The change from the roller ball mill to the more energetic vibratory mill was necessary due to the increased viscosity of the mixture, especially during the initial stage of mixing when the powder was not well dispersed. The viscosity of each composition was analyzed using the rotational viscometer, as described in the previous sections. Then, 2 wt% of photoinitiator (in relation to the monomer) was added to the suspension and mixed for additional 2 h in the vibratory mill. The cured thickness of each composition was measured for exposures of 1, 2, 3, and 5 s. Printing tests were performed with the formulations with 35 and 40 vol% $CaCO_3$ loading. Additionally, a stability test was performed with the formulations in a graduated tube for 30 days to assess the sedimentation of the systems.

### 2.3. 3D printing

The final formulation was prepared with PEGDA 250 as the monomer, 35 vol% of $CaCO_3$ powder (equivalent to 56 wt%), 2 wt% (in relation to the $CaCO_3$ powder) of Solsperse 85000 as the dispersant, and 2 wt% (in relation to the monomer) of phenylbis(2,4,6-trimethyl benzoyl)phosphine oxide as the photoinitiator. The components were mixed without the photoinitiator for 10 h in the vibration ball mill. After adding the photoinitiator, the suspension was mixed for additional 2 h.

Additive manufacturing was performed with a bottom-up mask-projection vat-photopolymerization 3D printer (Creality LD-002H), which has an LCD as the light source operating with a wavelength of 405 nm and an intensity of 8 mW/cm$^2$. The layer height was defined as 50 μm, and the curing time was set to 1 s per layer. Different geometries for possible applications of calcium carbonate parts were produced, including scaffolds, coral-like structures, and a 2D fluid device to study the fluid displacement in rock models.

### 2.4. Debinding and sintering

One printed sample was ground and characterized through simultaneous thermogravimetric analysis (TGA) and differential scanning calorimetry (DSC) (TGA/DSC 3+ Star$^e$ system - Mettler Toledo). The program was set from room temperature to 1000 °C, with a heating rate of 5 °C/min and airflow of 100 mL/min. The initial weight of the sample was 34,6589 mg.

The debinding heating rates were adjusted so the slow heating rates would coincide with the peaks of the decomposition of PEGDA measured through the TGA, which occurs more intensely between 350 and 440 °C (as also observed in Ref. [110]). The debinding was performed in the Lindberg/Blue M Box Furnace following the program depicted in Fig. 3 in air atmosphere, followed by natural cooling inside the furnace chamber.

After the debinding, the samples were transferred to a tubular furnace (The construction of the furnace is detailed elsewhere [1]). Sintering was performed according to the heating program reported in Table 1. Initially, compressed air was injected into the furnace at ≈3 L/min. Then, above 500 °C, the gas flow was switched to $CO_2$ (≈3 L/min) to avoid the decomposition of the calcium carbonate [1].

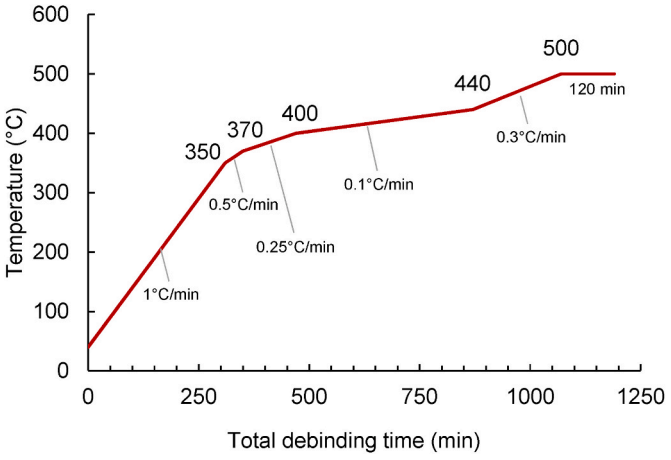


**Fig. 3.** Debinding program.

**Table 1**
Sintering program.

| Step | Gas flow | $T_{start}$ | $T_{end}$ | Rate | Step time | Total time |
|---|---|---|---|---|---|---|
| | | °C | °C | °C/min | min | min |
| 1 | Air | 20 | 500 | 1 | 480 | 480 |
| 2 | Air | 500 | 500 | – | 120 | 600 |
| 3 | $CO_2$ | 500 | 820 | 5 | 64 | 664 |
| 4 | $CO_2$ | 820 | 850 | 2 | 15 | 679 |
| 5 | $CO_2$ | 850 | 850 | – | 120 | 799 |
| 6 | $CO_2$ | 850 | 500 | furnace natural cooldown | | |
| 7 | – | 500 | 30 | | | |

### 2.5. Characterization of 3D printed and sintered samples

#### 2.5.1. X-ray diffraction

The crystalline phase assemblage of the materials was evaluated using X-Ray diffraction (XRD). The analyses were performed with the powder as supplied (pure calcite), after 3D printing, after debinding at 500 °C, and after sintering at 850 °C in a $CO_2$ atmosphere. All analyses were conducted using a Shimadzu XRD-7000 Maxima X with the following parameters: Cu $K_\alpha$ radiation, 40 kV, 30 mA, divergence and scatter slit of 1°, receiving slit of 0.3 mm, continuous scan θ-2θ with 2°/min ranging from 20 to 50°.

#### 2.5.2. Scanning electron microscopy

The 3D printed and sintered samples were fractured and coated with gold (G20 ion sputter coater). The images were acquired using an EmCrafts CUBE Scanning Electron Microscopy with a secondary electron (SE) detector using an accelerating voltage of 10 kV.

## 3. Results and discussion

### 3.1. Calcium carbonate suspension

#### 3.1.1. Selecting the monomer

The viscosity of the suspensions with variable content of PEGDA and HEMA at a shear rate of 30 s$^{-1}$ are reported in Fig. 4. An unexpected behavior was found concerning the effect of monomer content. Although the suspension with 100% HEMA has a lower viscosity than the suspension with 100% PEGDA, adding a small amount of HEMA (5 or 10%) increased the viscosity of the mixture. On the other hand, mixtures with a larger amount of HEMA (33 or 67%) presented viscosities lower than each of the original components. The explanation for this phenomenon is beyond the scope of this paper and requires further investigation. It might be the case that the solubility and wettability between the monomers have a significant effect on the dispersion of the material and

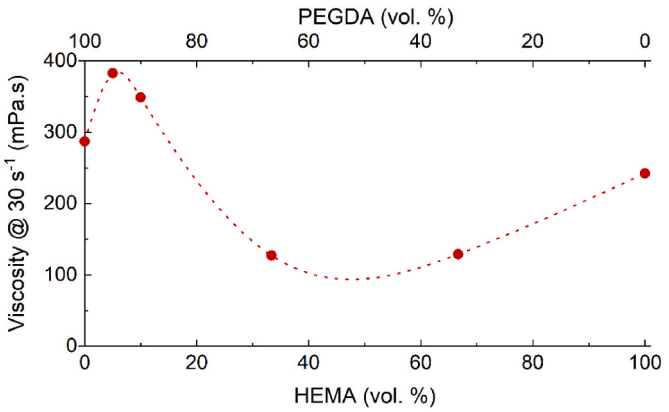


**Fig. 4.** Effect of the concentration of the monomers PEGDA and HEMA in the viscosity of a suspension with 15 vol% of $CaCO_3$. The sum of the volumetric content of HEMA + PEGDA is 100% of the liquid content.

the consequent rheological properties. For the purpose of this study, reducing the viscosity of the suspension would require a large amount of HEMA because adding only a small amount has a detrimental effect and should be avoided.

Concerning the cured thickness, it was observed that adding HEMA reduced the photoreactivity of the suspension, increasing the curing time (Fig. 5). The samples with 5 and 10 vol% of HEMA had insufficient curing with 1 and 2s, being able to cure only with 5s or more. Suspensions with even more HEMA required more time (>10 s) or didn't cure at all (within the evaluated times). The measured suspensions had only 15 vol% of ceramic powder, which is relatively low. Adding more powder would reduce even more the cured thickness because the particles cause light scattering (which requires longer curing times) [101,103]. Hence suspensions with more than 10% of HEMA would require a long time to cure each layer (>>10 s) and would have a low resolution (larger minimum layer thickness), which would be undesirable for additive manufacturing. Therefore, considering only the effect on the cured thickness, adding HEMA should be limited up to 10 vol%. In conclusion, HEMA was not further used in this study because it would be detrimental both for the viscosity and the cured thickness. Hence, pure PEGDA 250 was chosen as the monomer.

### 3.1.2. Selecting the dispersant

The viscosity of the suspensions with different dispersants is shown in Fig. 6. The dispersant Solsperse 85000 (a phosphodiester polymeric dispersant) had the best result among the compared ones. Therefore, it was used in the subsequent steps of this research. Solsperse 41000 (a

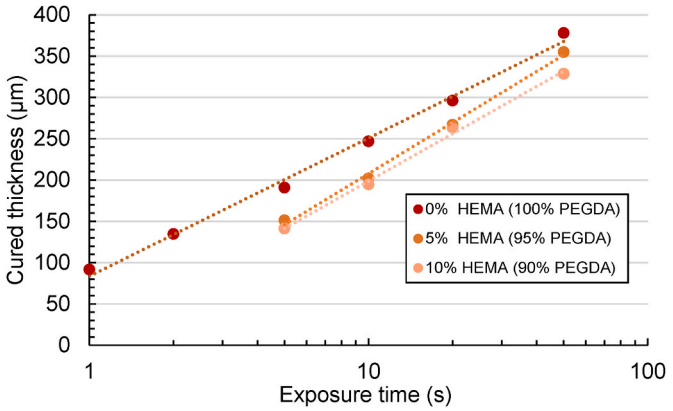


**Fig. 5.** Effect of the monomer content on the cured thickness. Samples with more than 10% of HEMA had insufficient curing and were not included in the graph.

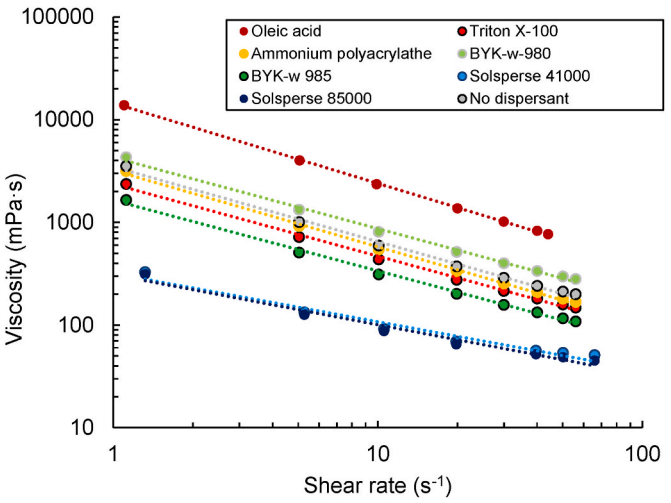


**Fig. 6.** Comparison of the effect of several dispersants on the viscosity of a suspension with 15 vol% of $CaCO_3$ in PEGDA 250 monomer. The suspension with the dispersant BYK-966 foamed too much and could not be measured.

polymeric alkoxylate dispersant) also had very good results. On the other hand, some dispersants had a detrimental effect. Some of them (Byk w-980 and Byk w-966, which are solutions of a salt of unsaturated polyamine amides and acidic polyesters) seemed to facilitate the formation of bubbles, increasing the overall apparent viscosity. The worst situation was found for oleic acid, which significantly increased the viscosity of the suspension. In addition, the amount of dispersant seemed unoptimized, leading to some flocculation.

### 3.1.3. Selecting the solid loading

The viscosity of the suspensions with different solid loadings is shown in Fig. 7. It can be observed that all suspensions had a shear-thinning behavior that could be fitted with the power-law viscosity model (Eq. 1) [113], where $\mu$ is the suspension viscosity, $\dot{\gamma}$ is the shear rate, $K$ and $n$ are the fitting parameters (flow consistency and flow behavior indexes, respectively). The fitted parameters and the R-squared of the regression for each solid loading are displayed in Table 2, where $\varphi$ is the volumetric solid loading. The measurement of the suspension with 50 vol% appeared to suffer from slipping effects resulting in an underestimation of the viscosity and an apparent increased shear-thinning behavior.

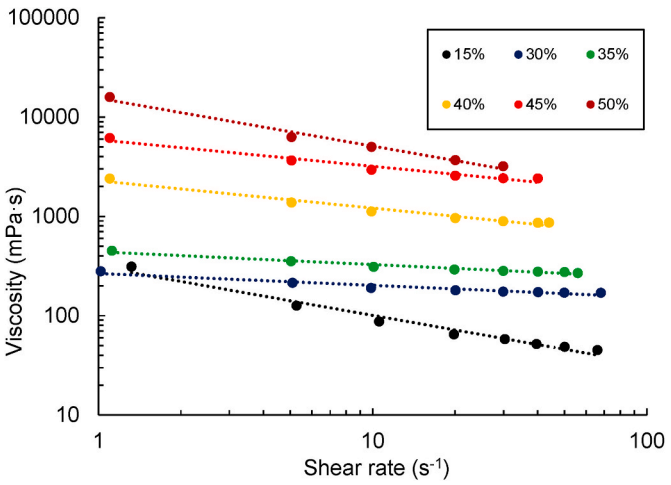


**Fig. 7.** Viscosity of the suspensions with different solid volumetric loadings. All of them follow a shear-thinning behavior. Viscosity curves were fitted with the power-law model.

**Table 2**
Coefficients of the power-law model and the R-square of the regression.

| $\varphi$ | $K$ | $n$ | $R^2$ |
|---|---|---|---|
| 15% | 310.2 | 0.511 | 0.983 |
| 30% | 266.0 | 0.881 | 0.950 |
| 35% | 439.7 | 0.872 | 0.972 |
| 40% | 2284 | 0.725 | 0.978 |
| 45% | 5902 | 0.733 | 0.977 |
| 50% | 15458 | 0.517 | 0.990 |

$$\mu = K\dot{\gamma}^{n-1} \quad \text{(Eq. 1)}$$

Increasing the solid loading had an exponential effect on the viscosity, as shown in Fig. 8. The data could be fitted by the Krieger-Dougherty model (Eq. 2) [87,114], which relates the suspension viscosity $\mu$ to the volumetric solid loading $\varphi$. In the equation, $\mu_0$ is the medium viscosity, $\varphi_{max}$ is the maximum volumetric solid loading, and $B$ is the "intrinsic viscosity" or Einstein's coefficient. The nominal viscosity of the PEGDA 250 (15 mPa s) was adopted as the medium viscosity ($\mu_0$). The fitted parameters were $\varphi_{max} = 0.598$ and $B = 6.09$, with a R-square of 0.997.

$$\mu = \mu_0 \left(1 - \varphi/\varphi_{max}\right)^{-B\varphi_{max}} \quad \text{(Eq. 2)}$$

The suspension with 35 vol% of $CaCO_3$ had a very low viscosity (0.28 Pa s at 30s $^{-1}$), which could be successfully printed in the ordinary bottom-up 3D printer used in this research. Although the suspensions with 40 and 45 %vol of $CaCO_3$ had low viscosity (0.89 and 2.41 Pa s at 30 $s^{-1}$, respectively), the absence of a recoating mechanism in the used printer resulted in failed parts due to vat-sticking (parts detached from the building platform). In conclusion, the upper limit for the suitable viscosity at 30 $s^{-1}$ is between 0.28 and 0.89 Pa s for this type of 3D printer. The samples with 35 vol% or more solid loading presented little sedimentation after 30 days (less than 2%), indicating the stability of the formulations.

Concerning the photoreactivity, the cured thickness of the suspensions with 35 and 40 vol% are reported in Fig. 9. They follow the Beer-Lambert law (Eq. 3), where $C_d$ is the cured thickness, $D_p$ is the penetration depth, $E$ is the irradiated energy, and $E_c$ is the critical exposure energy to form a layer [101,103,115]. The fitted parameters can be found in Table 3. The cured depth for 1 s exposure for the 35 and 40 vol % suspensions were 96.3 and 86.0 μm, respectively. As expected, increasing the solid loading led to a smaller cured thickness [101,116].

$$C_d = D_p \ln\left(E/E_c\right) \quad \text{(Eq. 3)}$$

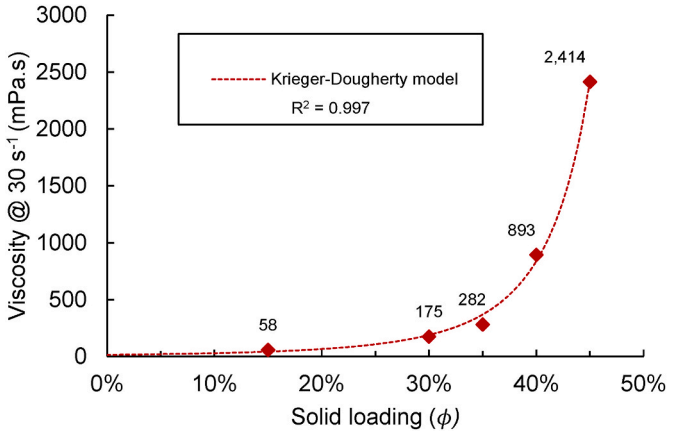


**Fig. 8.** Effect of solid loading on the viscosity of the $CaCO_3$ suspensions at a shear rate of 30 $s^{-1}$. Data fitted with the Kriger-Dougherty model.

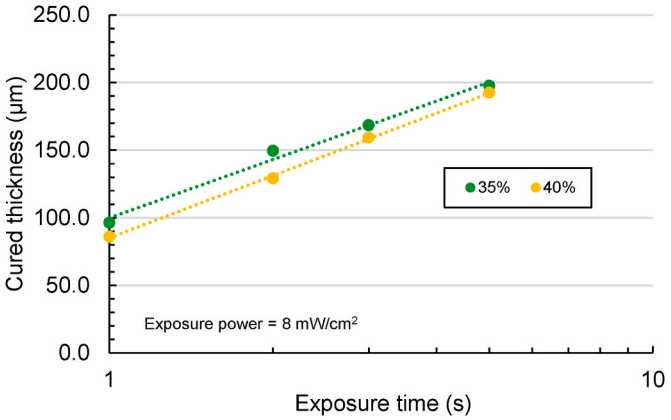


**Fig. 9.** Cured thickness for suspensions with 35 and 40 vol% solid loadings. The curves were fitted with the logarithmic model (Beer-Lambert law).

**Table 3**
Coefficients of the Beer-Lambert model and the R-square of the regression for the suspensions with 35 and 40 vol%.

| $\varphi$ | $C_d$ (at 1 s) | $D_p$ | $E_c$ | $R^2$ |
|---|---|---|---|---|
| % | μm | μm | mJ/cm$^2$ | – |
| 35 | 96.3 | 439.7 | 1.608 | 0.972 |
| 40 | 86.0 | 2284 | 2.224 | 0.978 |

### 3.2. 3D printed parts

3D printing was successfully performed with the 35 vol% $CaCO_3$ resin. Some of the produced parts are displayed in Fig. 10. The excellent resolution achieved should be highlighted, as evidenced by the fine details reproduced, which can be observed in Fig. 11.

The selection of a layer thickness of 50 μm and a curing time of 1s (equivalent to a cured layer of 96.3 μm) resulted in a cured-layer-to-layer-thickness ratio of about 2, which was found to be a good compromise between printing resolution and strong adhesion between layers. In the SEM images, the interface between the layers could hardly be observed in the interior of fractured samples (Fig. 12).

### 3.3. Debinding and sintering

The TGA/DSC of a printed sample is displayed in Fig. 13. From the graph, two main events can be observed. One is the exothermic decomposition of the polymeric component. The mass loss starts at about 240 °C and finishes at about 480 °C, with the main peak of mass loss at 421 °C. As observed, practically all the organic constituents can be eliminated below 500 °C during the debinding stage. The second event is the endothermic decomposition of the calcium carbonate into calcium oxide, starting at about 590 °C and ending at about 800 °C. This decomposition was expected to happen in an air atmosphere but would be avoided in a $CO_2$ atmosphere. Therefore, because the two events were not overlapping, the strategy of switching from air to a $CO_2$ atmosphere above 500 °C proved to be suitable for the process.

Actually, the samples after debinding were slightly gray (Fig. S2, in the Supplementary Material), as some residual carbon remained in the parts. But the parts turned white at the end of sintering, indicating that the remaining carbon was eliminated.

The sintered parts are displayed in Fig. 14. The parts retained their geometry, especially the ones with thinner walls and cross sections (Fig. 14A and B). However, the debinding stage used in this work was still too fast. Consequently, some parts also presented cracks and delamination problems (Fig. 14C and D). Remarkably, the CAD-designed scaffolds suffered from some delamination at the interfaces,

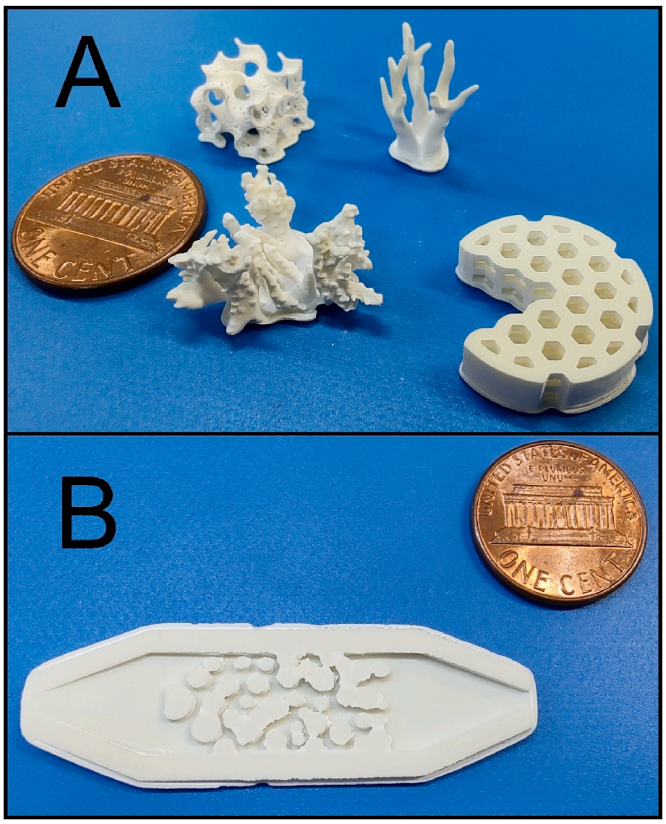


**Fig. 10.** 3D printed samples of calcium carbonate (before sintering). In A, a gyroid, a CAD-designed scaffold, and two coral-like structures. In B, a proposal of a 2D fluidic device with a geometry resembling the porous channels of rock for fluid displacement studies. The coin used as a reference has a diameter of 19 mm.

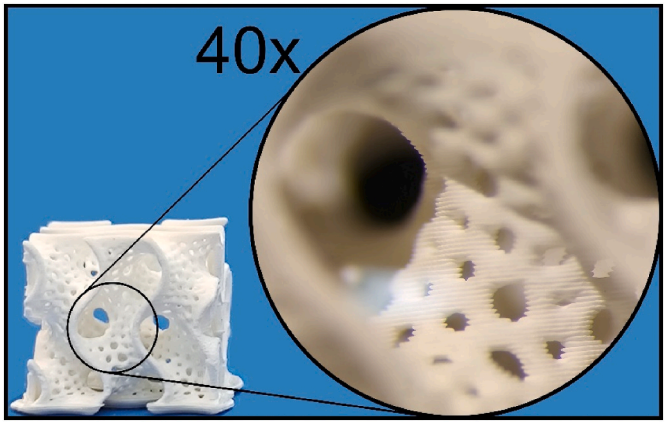


**Fig. 11.** 3D printed gyroid scaffold (before sintering) with detailed view obtained with an optical microscope at 40x magnifications. The layers and the small designed pores are visible. The diameters of the small pores are ~300–500 μm.

where there was an abrupt change in the cross-section area. Evidently, the volumetric content of the photopolymer was considerably high and the debinding rate was too fast for these geometries.

The scanning electron microscopy revealed that even very small details were retained during sintering, such as the small pores observed in the gyroid scaffold structure (Fig. 15A and B). Moreover, the submicrometric needle-like particles observed in the original powder (Fig. 2) were sintered into larger rounded grains with a diameter of

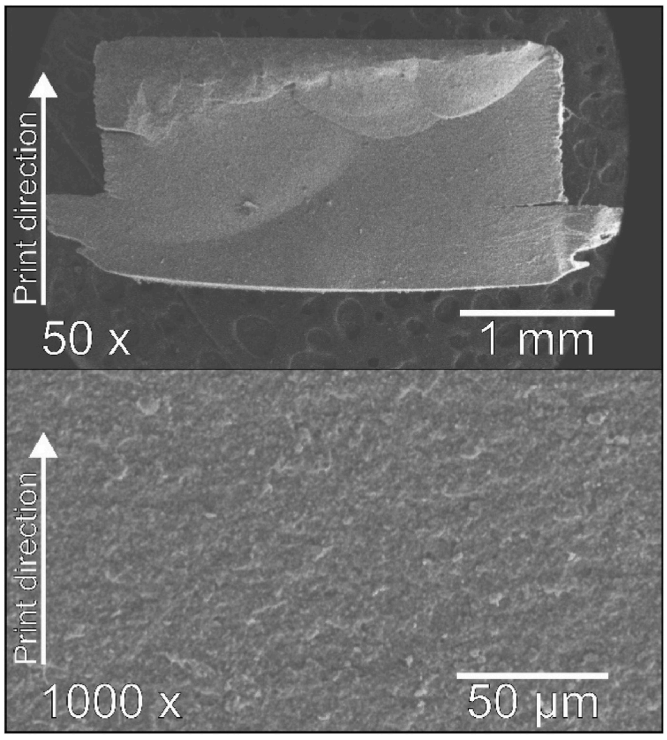


**Fig. 12.** Scanning Electron Microscopy of a fractured 3D printed bar (before sintering). The upper image has 50x magnification, and the lower image has 1000x magnification. The arrows indicate the printing direction.

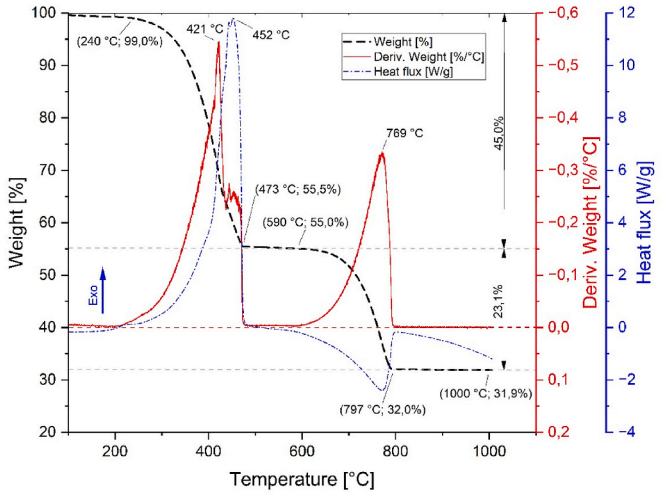


**Fig. 13.** TGA/DSC of a 3D printed sample. From room temperature to 1000 °C at 5 °C/min with airflow of 100 mL/min.

about 1–2 μm (Fig. 15C). Nevertheless, the structure was still porous, and the grains seemed weakly bonded. Therefore, due to the porosity and the cracks induced during the debinding stage, the mechanical resistance of the parts was low (fragile to handling).

The proposed manufacturing strategy successfully retained the calcite phase throughout the process, as confirmed by the XRD patterns (Fig. 16). Only the peaks of the calcite crystalline phase were identified through all the stages of the processing. If thermal decomposition had occurred during sintering, there would be peaks in the diffractogram related to calcium oxide or calcium hydroxide. Therefore, sintering using a $CO_2$ atmosphere prevented the decomposition of $CaCO_3$ and the formation of CaO, enabling also its sintering.

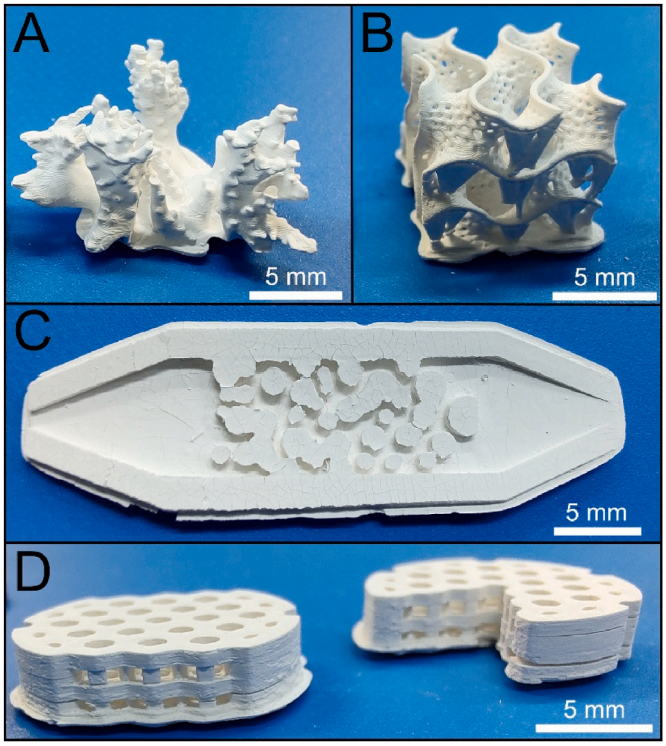


**Fig. 14.** Sintered parts. A) Coral-like structure; B) Gyroid scaffold; C) Bidimensional "porous" fluidic device for biphasic fluid displacement studies; D) CAD-designed scaffolds.

### 3.4. Discussion: opportunities, challenges, and next steps

This work enabled to obtain ceramic suspensions with very low viscosity at 30 $s^{-1}$ (0.28, 0.89, and 2.41 Pa s at 35, 40, and 45 vol% $CaCO_3$ loading, respectively), comparable to the best results found in literature for other ceramic materials (0.2–0.5 Pa s for 40 vol% and 1.2–2.3 Pa s for 45 vol%) [87,103]. Furthermore, the solid loadings achieved are higher than previously described in literature for calcium carbonate photopolymerization (29.5 vol%) [6]. Selecting an appropriate dispersant was a crucial aspect of the process, reducing the viscosity to about 20% of the original value without a dispersant. The resolution of the printing process was excellent, being able to reproduce very small pores (with a diameter of 300 μm) and features, as shown in Figs. 10, 11, and 15. Additionally, the strategy of debinding in air followed by sintering in $CO_2$ resulted in parts comprised of 100% calcium carbonate.

As stated in the introduction, 3D-printed calcium carbonate parts have a very similar chemical constitution to corals and carbonate rocks and could also have an important application as bone scaffolds. Therefore, for future studies, the viability of using such calcium carbonate parts produced by vat-photopolymerization for these potential applications could be explored. Furthermore, considering the use of 3D-printed artificial rocks for petrophysical tests, the individual effect of each geometrical feature of the samples (such as porosity, pore size distribution, and shape) on significant properties (such as permeability and liquid absorption) could be explored in a replicable manner.

Nevertheless, some points still need improvement and additional studies. First, using a conventional bottom-up DLP printer without a recoating system restricted the use of suspensions with a larger ceramic content. Using a 3D printer more suited to higher viscosity resins (such as top-down 3D printers or the ones with recoating system and vat separation mechanisms) would allow adopting higher solid loadings, reducing the debinding problems and increasing the density and mechanical resistance of the printed parts.

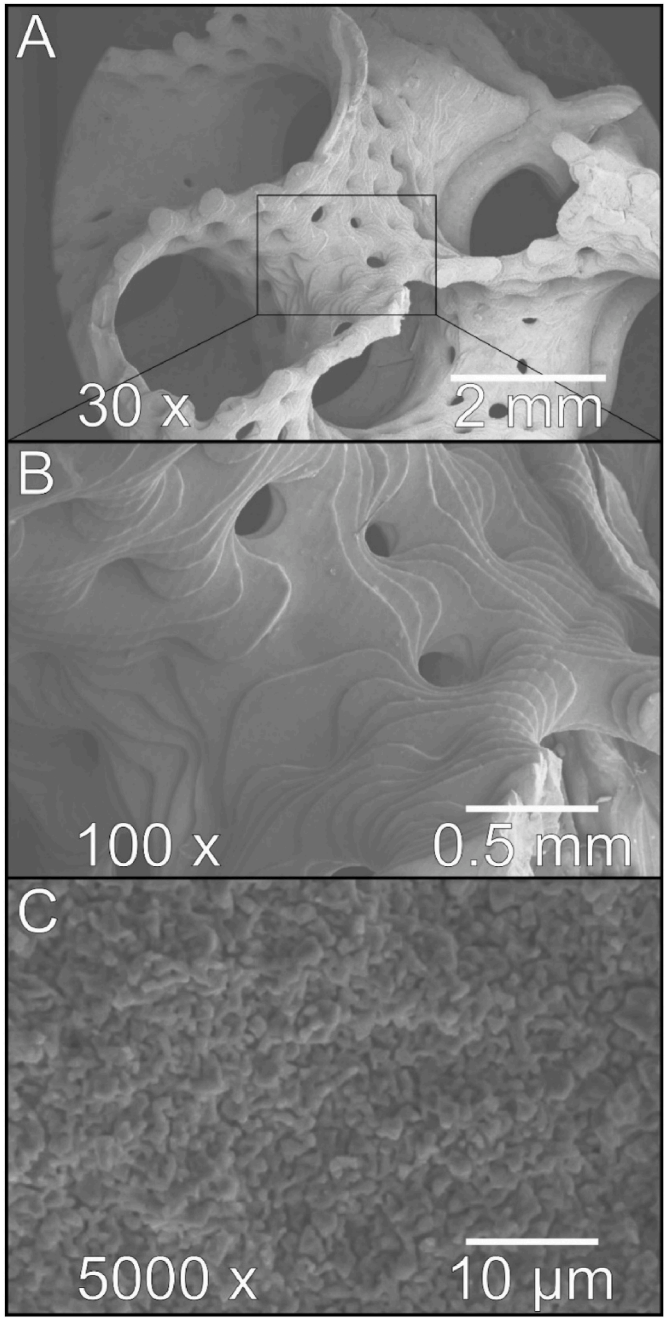


**Fig. 15.** Scanning Electron Microscopy of 3D printed samples after sintering in a $CO_2$ atmosphere. A) and B) are the gyroid scaffold with 30x and 100x magnification, respectively. C) is the cross-section of a fractured sample.

Secondly, the debinding rate and layer thickness still need to be optimized. The debinding of larger parts would require slower heating rates and longer dwell times for adequate removal of the gases produced by the organic burn-out without stressing and cracking the ceramic matrix. As a matter of fact, the debinding stage is currently the major bottleneck of the additive manufacturing of conventional ceramics through photopolymerization. The state-of-art still limits the debinding to parts with up to ~10 mm wall thickness [91]. This limit might not be problematic for porous bone scaffolds, coral-like structures, or microfluidic devices. However, for artificial rock replicas for petrophysical tests, this might be a very significant technological restriction, as the samples (called core plugs) for many petrophysical tests commonly have 25–51 mm (1–2 inches) of diameter and height [15]. Therefore, alternatives more suitable for larger parts should be evaluated for this type of

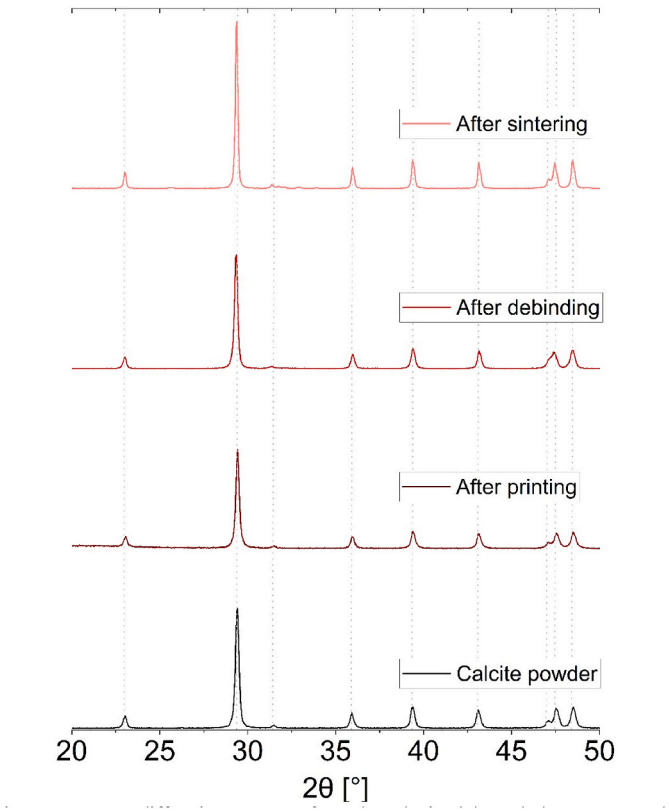


**Fig. 16.** X-Ray diffraction patterns of powders obtained through the process. Only calcite peaks were observed (indicated by the vertical lines). The peaks were compared with the reference diffractogram of calcite obtained from the Inorganic Crystal Structure Database (ICSD) (compound 191852 [28]).

application, such as slip casting [11]; gel-casting [4,117]; casting with geopolymers [118]; or other additive manufacturing technologies such as Binder Jetting [51,64,71] or Material Extrusion (Direct Ink Writing or Robocasting) [105,106].

## 4. Conclusions

A photocurable calcium carbonate resin was successfully formulated with a 35 vol% loading. The slurries obtained possessed a very low viscosity (0.28 Pa s at 30 $s^{-1}$) and suitable cured thickness (96 μm for 1 s) through the proper selection of the monomer and dispersant. The calcium carbonate suspension was used to print parts with high resolution, including scaffolds, bidimensional fluidic devices, and artificial corals using an ordinary bottom-up vat-photopolymerization 3D printer. Furthermore, by using proper atmosphere control (air during debinding and $CO_2$ during sintering), it was possible to completely remove the organics and sinter $CaCO_3$ without thermal decomposition. The presented results are an important advance for fabricating pure calcium carbonate parts with complex geometries that can be used as bone scaffolds, coral restorations, artificial rocks, and other applications.

## Funding

This work was supported by the São Paulo Research Foundation (FAPESP) [grants # 2020/16012-1 and #2021/12556-0], and the National Council for Scientific and Technological Development (CNPq) [grant #140797/2020-3].

## Data availability

The data that support the findings of this study are available from the corresponding author, Mateus M. Morais, upon request.

## CRediT author statement

Mateus M Morais: Conceptualization; Experimental investigation; Writing (Original draft); Italo L de Camargo: Conceptualization; Methodology; Experimental investigation; Writing (Reviewing & editing); Paolo Colombo: Supervision; Resources; Writing (Reviewing & editing); Carlos A Fortulan: Writing (Reviewing & editing); Supervision; Project administration.

## Declaration of competing interest

The authors declare that they have no known competing financial interests or personal relationships that could have appeared to influence the work reported in this paper.

## Acknowledgements

We would like to acknowledge Prof. Dr. Eduardo Bellini Ferreira and Prof. Rafael Salomão from USP for granting access to the viscosimeter, BET and pycnometer facilities and LMA-IQ from UNESP for FEG-SEM facilities. Additionally, we would like to thank the companies Lubrizol and BYK for supplying dispersant samples.

## Appendix A. Supplementary data

Supplementary data to this article can be found online at https://doi.org/10.1016/j.oceram.2023.100348.

## References

[1] M.M. Morais, R.D. Salomão, C.A. Fortulan, Successful and failed attempts to obtain bulk calcium carbonate parts through sintering and carbonation, in: Proceedings of the 65º-66º Congresso Brasileiro de Cerâmica, Associação Brasileira de Cerâmica, Águas de Lindóia, SP, 2022.
[2] H.-P. Mattila, R. Zevenhoven, Production of Precipitated Calcium Carbonate from Steel Converter Slag and Other Calcium-Containing Industrial Wastes and Residues, 2014, pp. 347–384, https://doi.org/10.1016/B978-0-12-420221-4.00010-X.
[3] F. Jiang, L. Zhang, Z. Jiang, C. Li, D. Cang, X. Liu, Y. Xuan, Y. Ding, Diatomite-based porous ceramics with high apparent porosity: pore structure modification using calcium carbonate, Ceram. Int. 45 (2019) 6085–6092, https://doi.org/10.1016/j.ceramint.2018.12.082.
[4] A.F. Lemos, J.M.F. Ferreira, Porous bioactive calcium carbonate implants processed by starch consolidation, Mater. Sci. Eng. C 11 (2000) 35–40, https://doi.org/10.1016/S0928-4931(00)00134-X.
[5] T.S. Putri, K. Hayashi, K. Ishikawa, Fabrication of three-dimensional interconnected porous blocks composed of robust carbonate apatite frameworks, Ceram. Int. 46 (2020) 20045–20049, https://doi.org/10.1016/j.ceramint.2020.05.076.
[6] H. Elsayed, M. Picicco, L. Ferroni, C. Gardin, B. Zavan, E. Bernardo, Novel bioceramics from digital light processing of calcite/acrylate blends and low temperature pyrolysis, Ceram. Int. 46 (2020) 17140–17145, https://doi.org/10.1016/j.ceramint.2020.03.277.
[7] F. He, F. Yang, J. Zhu, Y. Peng, X. Tian, X. Chen, Fabrication of a novel calcium carbonate composite ceramic as bone substitute, J. Am. Ceram. Soc. 98 (2015) 223–228, https://doi.org/10.1111/jace.13285.
[8] G. Tarì, J.M.F. Ferreira, Colloidal processing of calcium carbonate, Ceram. Int. 24 (1998) 527–532, https://doi.org/10.1016/S0272-8842(97)00052-7.
[9] F. He, W. Ren, X. Tian, W. Liu, S. Wu, X. Chen, Comparative study on in vivo response of porous calcium carbonate composite ceramic and biphasic calcium phosphate ceramic, Mater. Sci. Eng. C 64 (2016) 117–123, https://doi.org/10.1016/j.msec.2016.03.085.
[10] A. Otsu, K. Tsuru, M. Maruta, M.L. Munar, S. Matsuya, K. Ishikawa, Fabrication of microporous calcite block from calcium hydroxide compact under carbon dioxide atmosphere at high temperature, Dent. Mater. J. 31 (2012) 593–600, https://doi.org/10.4012/dmj.2011-252.
[11] F. Monchau, P. Hivart, B. Genestie, F. Chai, M. Descamps, H.F. Hildebrand, Calcite as a bone substitute. Comparison with hydroxyapatite and tricalcium phosphate with regard to the osteoblastic activity, Mater. Sci. Eng. C 33 (2013) 490–498, https://doi.org/10.1016/j.msec.2012.09.019.
[12] H.I. Albalawi, Z.N. Khan, A.U. Valle-Pérez, K.M. Kahin, M. Hountondji, H. Alwazani, S. Schmidt-Roach, P. Bilalis, M. Aranda, C.M. Duarte, C.A.E. Hauser, Sustainable and eco-friendly coral restoration through 3D printing and

fabrication, ACS Sustain. Chem. Eng. 9 (2021) 12634–12645, https://doi.org/10.1021/acssuschemeng.1c04148.
[13] J.W. Anthony, R.A. Bideaux, K.W. Nichols, C.M. Bladh, Handbook of Mineralogy, V, Borates, Carbonates, Sulfates, Mineralogical Society of America, Chantilly, VA, 2003.
[14] S. Ishutov, T.D. Jobe, S. Zhang, M. Gonzalez, S.M. Agar, F.J. Hasiuk, F. Watson, S. Geiger, E. Mackay, R. Chalaturnyk, Three-dimensional printing for geoscience: fundamental research, education, and applications for the petroleum industry, Am. Assoc. Petrol. Geol. Bull. 102 (2018) 1–26, https://doi.org/10.1306/0329171621117056.
[15] J.J.A. Florez, J.V. Ferrari, M. Michelon, C. Ulsen, Construction of synthetic carbonate plugs: a review and some recent developments, Oil Gas Sci. Technol. 74 (2019), https://doi.org/10.2516/ogst/2019001.
[16] J.J.A. Florez, J.V. Ferrari, Preliminary analyses of synthetic carbonate plugs: consolidation, petrophysical and wettability properties, Oil Gas Sci. Technol. 76 (2021) 12, https://doi.org/10.2516/ogst/2020087.
[17] A.G. Almetwally, H. Jabbari, Experimental investigation of 3D printed rock samples replicas, J. Nat. Gas Sci. Eng. 76 (2020), 103192, https://doi.org/10.1016/j.jngse.2020.103192.
[18] L. Kong, M. Ostadhassan, B. Liu, C. Li, K. Liu, Multifractal Characteristics of MIP-Based Pore Size Distribution of 3D-Printed Powder-Based Rocks: A Study of Post-Processing Effect, 129, Transp Porous Media, 2019, pp. 599–618, https://doi.org/10.1007/s11242-018-1152-9.
[19] L. Kong, M. Ostadhassan, X. Hou, M. Mann, C. Li, Microstructure characteristics and fractal analysis of 3D-printed sandstone using micro-CT and SEM-EDS, J. Pet. Sci. Eng. 175 (2019) 1039–1048, https://doi.org/10.1016/j.petrol.2019.01.050.
[20] S. Ishutov, F.J. Hasiuk, D. Jobe, S. Agar, Using resin-based 3D printing to build geometrically accurate proxies of porous sedimentary rocks, Groundwater 56 (2018) 482–490, https://doi.org/10.1111/gwat.12601.
[21] L. Kong, S. Ishutov, F. Hasiuk, C. Xu, 3D printing for experiments in petrophysics, rock physics, and rock mechanics: a review, SPE Reservoir Eval. Eng. 24 (2021) 721–732, https://doi.org/10.2118/206744-pa.
[22] M.N. D'Eurydice, E.T. Montrazi, C.A. Fortulan, T.J. Bonagamba, T 2 -filtered T 2 − T 2 exchange NMR, J. Chem. Phys. 144 (2016), 204201, https://doi.org/10.1063/1.4951712.
[23] C. Cardoso, E. Lucas, B. Uwe, C. Alberto, T. José, A model system based on synthetic rocks for morphological studies in porous media, in: Proceeding of the 14th International Bologna Conference on Magnetic Resonance in Porous Media (MRPM14), 2018, p. P3. Gainesville, Florida, USA.
[24] C. Delle Piane, M.B. Clennell, J. Dautriat, G. Price, Fluid/rock interactions in porous carbonate rocks: an integrated mechanical, ultrasonic and micro-structural study, in: International Conference and Exhibition, Melbourne, Australia 13-16 September 2015, Society of Exploration Geophysicists and American Association of Petroleum Geologists, 2015, https://doi.org/10.1190/ice2015-2210005, 204–204.
[25] A. el Husseiny, T. Vanorio, The effect of micrite content on the acoustic velocity of carbonate rocks, Geophysics 80 (2015) L45–L55, https://doi.org/10.1190/geo2014-0599.1.
[26] Z. Wang, R. Wang, F. Wang, H. Qiu, T. Li, Experiment study of pore structure effects on velocities in synthetic carbonate rocks, Geophysics 80 (2015) D207–D219, https://doi.org/10.1190/geo2014-0366.1.
[27] Z. Wang, R. Wang, T. Li, M. Zhao, The combined effects of pore structure and pore fluid on the acoustic properties of cracked and vuggy synthetic rocks, J. Pet. Sci. Eng. 156 (2017) 202–211, https://doi.org/10.1016/j.petrol.2017.05.023.
[28] R.M. Fedrizzi, M.A.R. de Ceia, R.M. Misságia, V.H. Santos, I. Lima Neto, Artificial carbonate rocks: synthesis and petrophysical characterization, J. Pet. Sci. Eng. 163 (2018) 303–310, https://doi.org/10.1016/j.petrol.2017.12.089.
[29] W. Wang, S. Chang, A. Gizzatov, Toward reservoir-on-a-chip: fabricating reservoir micromodels by in situ growing calcium carbonate nanocrystals in microfluidic channels, ACS Appl. Mater. Interfaces 9 (2017) 29380–29386, https://doi.org/10.1021/acsami.7b10746.
[30] A. Kanjirakat, A. Belaidi, A. Carvero, M. Amani, A. Retnanto, Surface Modification of Stereolithography-Based 3D Printed Structures Utilizing Ultrasonic-Atomised Sprays, 2022, https://doi.org/10.21203/rs.3.rs-2335901/v1.
[31] N. Alyafei, R. al Musleh, J. Bautista, M. Idris, T. Seers, Enhanced learning of fundamental petrophysical concepts through image processing and 3D printing, Petrophysics 62 (2021) 463–476, https://doi.org/10.30632/pjv62n5-2020a2.
[32] A. Patmonoaji, M.A. Mahardika, M. Nasir, Y. She, W. Wang, M.A. Muflikhun, T. Suekane, Stereolithography 3D printer for micromodel fabrications with comprehensive accuracy evaluation by using microtomography, Geosciences 12 (2022) 183, https://doi.org/10.3390/geosciences12050183.
[33] A.S. Zakaria, H.A. Nasr-El-Din, M. Ziauddin, Flow of emulsified acid in carbonate rocks, Ind. Eng. Chem. Res. 54 (2015) 4190–4202, https://doi.org/10.1021/ie504167y.
[34] C.R. dos S Lucas, Y.K.P.G. Aum, E. de A. Araújo, T.N. de Castro Dantas, E. A. Araújo, T.N. Sousa, P.T.P. Aum, Investigating the fluid–solid interaction of acid nonionic nanoemulsion with carbonate porous media, Molecules 25 (2020) 1475, https://doi.org/10.3390/molecules25061475.
[35] T.N. de Castro Dantas, A.C. de Oliveira, T.T.C. de Souza, C.R. dos Santos Lucas, E. de Andrade Araújo, P.T.P. Aum, Experimental study of the effects of acid microemulsion flooding to enhancement of oil recovery in carbonate reservoirs, J. Pet. Explor. Prod. Technol. 10 (2020) 1127–1135, https://doi.org/10.1007/s13202-019-00754-x.
[36] R.O. Baker, H.W. Yarranton, J.L. Jensen, Conventional core analysis–rock properties, in: Practical Reservoir Engineering and Characterization, Elsevier, 2015, pp. 197–237, https://doi.org/10.1016/B978-0-12-801811-8.00007-9.
[37] A. Escardino, J. García-Ten, C. Feliu, A. Saburit, V. Cantavella, Kinetic study of the thermal decomposition process of calcite particles in air and CO2 atmosphere, J. Ind. Eng. Chem. 19 (2013) 886–897, https://doi.org/10.1016/j.jiec.2012.11.004.
[38] J.M. Criado, M. González, J. Málek, A. Ortega, The effect of the CO2 pressure on the thermal decomposition kinetics of calcium carbonate, Thermochim. Acta 254 (1995) 121–127, https://doi.org/10.1016/0040-6031(94)01998-V.
[39] R. Viswanathan, T.S.L. Narasimhan, S. Nalini, Study of incongruent decomposition of calcium carbonate by transpiration thermogravimetry, J. Chem. Eng. Data 55 (2010) 3779–3785, https://doi.org/10.1021/je100294t.
[40] J.M. Valverde, P.E. Sanchez-Jimenez, L.A. Perez-Maqueda, Limestone calcination nearby equilibrium: kinetics, CaO crystal structure, sintering and reactivity, J. Phys. Chem. C 119 (2015) 1623–1641, https://doi.org/10.1021/jp508745u.
[41] D.W. Richerson, W.E. Lee, Modern Ceramic Engineering, fourth ed., CRC Press, 2018 https://doi.org/10.1201/9780429488245.
[42] J.S. Reed, Principles of Ceramics Processing, second ed., John Wiley & Sons, New York, 1995.
[43] N. Someya, T. Kitazato, T. Fujikawa, Y. Manabe, Sintered Body of Calcium Carbonate and Process for Producing Same, Patent US 5187125A, 1993.
[44] E. Yasar, Y. Erdogan, Correlating sound velocity with the density, compressive strength and Young's modulus of carbonate rocks, Int. J. Rock Mech. Min. Sci. 41 (2004) 871–875, https://doi.org/10.1016/j.ijrmms.2004.01.012.
[45] P.W. Choquette, L.C. Pray, Geologic nomenclature and classification of porosity in sedimentary carbonates, AAPG (Am. Assoc. Pet. Geol.) Bull. 54 (1970) 207–250.
[46] R.G. Loucks, R.M. Reed, S.C. Ruppel, U. Hammes, Spectrum of pore types and networks in mudrocks and a descriptive classification for matrix-related mudrock pores, Am. Assoc. Petrol. Geol. Bull. 96 (2012) 1071–1098, https://doi.org/10.1306/08171111061.
[47] Y.H. Lee, J.W. Lee, S.Y. Yang, H. Lee, Y.H. Koh, H.E. Kim, Dual-scale porous biphasic calcium phosphate gyroid scaffolds using ceramic suspensions containing polymer microsphere porogen for digital light processing, Ceram. Int. 47 (2021) 11285–11293, https://doi.org/10.1016/j.ceramint.2020.12.254.
[48] A. Lucas, J.-F. Michel, J.-F. Gaude, C. Carel, Macro-Porous Composite Support for Medicinal Substance(s) That can be Used as a Bone Reconstitution Material and a Method of Producing it, Patent US 6322592 B2, 2001.
[49] U. Scheithauer, F. Kerber, A. Füssel, S. Holtzhausen, W. Beckert, E. Schwarzer, S. Weingarten, A. Michaelis, Alternative process routes to manufacture porous ceramics—opportunities and challenges, Materials 12 (2019) 663, https://doi.org/10.3390/ma12040663.
[50] E.C. Hammel, O.L.R. Ighodaro, O.I. Okoli, Processing and properties of advanced porous ceramics: an application based review, Ceram. Int. 40 (2014) 15351–15370, https://doi.org/10.1016/j.ceramint.2014.06.095.
[51] S. Ishutov, F.J. Hasiuk, S.M. Fullmer, A.S. Buono, J.N. Gray, C. Harding, Resurrection of a reservoir sandstone from tomographic data using three-dimensional printing, Am. Assoc. Petrol. Geol. Bull. 101 (2017) 1425–1443, https://doi.org/10.1306/11111616038.
[52] S. Ishutov, F.J. Hasiuk, C. Harding, J.N. Gray, 3D printing sandstone porosity models, Interpretation 3 (2015) SX49, https://doi.org/10.1190/INT-2014-0266.1. –SX61.
[53] S. Dande, R.R. Stewart, N. Dyaur, Effect of fluids on the elastic properties of 3D-printed anisotropic rock models, Petrophysics 62 (2021) 537–552, https://doi.org/10.30632/PJV62N5-2021a7.
[54] T. Wu, H. Zhao, Q. Xu, Y. Zhao, Optimal analysis of material ratio for artificial rock by 3D printing technique, Geomechanics Geoengin. 17 (2020) 260–268, https://doi.org/10.1080/17486025.2020.1739752.
[55] C. Jiang, G.F. Zhao, A preliminary study of 3D printing on rock mechanics, Rock Mech. Rock Eng. 48 (2015) 1041–1050, https://doi.org/10.1007/s00603-014-0612-y.
[56] A.G. Almetwally, H. Jabbari, 3D-Printing Replication of Porous Media for Lab-Scale Characterization Research, ACS Omega 6 (2021) 260–268, https://doi.org/10.1021/acsomega.0c04825.
[57] T. Zhou, J.B. Zhu, Identification of a suitable 3D printing material for mimicking brittle and hard rocks and its brittleness enhancements, Rock Mech. Rock Eng. 51 (2018) 765–777, https://doi.org/10.1007/s00603-017-1335-7.
[58] S. Osinga, G. Zambrano-Narvaez, R.J. Chalaturnyk, Study of geomechanical properties of 3D printed sandstone analogue, in: 49th US Rock Mechanics/Geomechanics Symposium 2015, 4, 2015, pp. 3137–3142.
[59] J.S. Gomez, R.J. Chalaturnyk, G. Zambrano-Narvaez, Experimental Investigation of the Mechanical Behavior and Permeability of 3D Printed Sandstone Analogues under Triaxial Conditions, 129, Transp Porous Media, 2019, pp. 541–557, https://doi.org/10.1007/s11242-018-1177-0.
[60] N. Ardila, G. Zambrano-Narvaez, R.J. Chalaturnyk, Wettability Measurements on 3D Printed Sandstone Analogues and its Implications for Fluid Transport Phenomena, 129, Transp Porous Media, 2019, pp. 521–539, https://doi.org/10.1007/s11242-018-1176-1.
[61] K.J. Hodder, J.A. Nychka, R.J. Chalaturnyk, Process limitations of 3D printing model rock, Prog. Addit. Manuf. 3 (2018) 173–182, https://doi.org/10.1007/s40964-018-0042-6.
[62] K. Hodder, S. Ishutov, A. Sanchez, G. Zambrano, R. Chalaturnyk, 3D Printing of Rock Analogues in Sand: A Tool for Design and Repeatable Testing of Geomechanical and Transport Properties, E3S Web of Conferences, 205, 2020, https://doi.org/10.1051/e3sconf/202020504014.

[63] R. Song, Y. Wang, S. Ishutov, G. Zambrano-Narvaez, K.J. Hodder, R. J. Chalaturnyk, S. Sun, J. Liu, R.P. Gamage, A comprehensive experimental study on mechanical behavior, microstructure and transport properties of 3D-printed rock analogs, Rock Mech. Rock Eng. 53 (2020) 5745–5765, https://doi.org/10.1007/s00603-020-02239-4.

[64] F. Gobbin, H. Elsayed, A. Italiano, J. Adrien, P. Colombo, E. Maire, Large scale additive manufacturing of artificial stone components using binder jetting and their X-ray microtomography investigations, Open Ceram. 7 (2021), 100162, https://doi.org/10.1016/j.oceram.2021.100162.

[65] A.G. Almetwally, H. Jabbari, CO2 huff-n-puff experimentation and numerical simulation for 3D printed rock samples, Int. J. Heat Mass Tran. 180 (2021), 121798, https://doi.org/10.1016/j.ijheatmasstransfer.2021.121798.

[66] K.J. Hodder, K. Craplewe, S. Ishutov, R. Chalaturnyk, Binder saturation as a controlling factor for porosity variation in 3D-printed sandstone, Petrophysics 62 (2021) 450–462, https://doi.org/10.30632/PJV62N5-2020a1.

[67] L. Kong, M. Ostadhassan, C. Li, N. Tamimi, Pore characterization of 3D-printed gypsum rocks: a comprehensive approach, J. Mater. Sci. 53 (2018) 5063–5078, https://doi.org/10.1007/s10853-017-1953-1.

[68] L. Kong, M. Ostadhassan, C. Li, N. Tamimi, Can 3-D printed gypsum samples replicate natural rocks? An experimental study, Rock Mech. Rock Eng. 51 (2018) 3061–3074, https://doi.org/10.1007/s00603-018-1520-3.

[69] F.J. Hasiuk, Testing Bulk Properties of Powder-Based 3D-Printed Reservoir Rock Proxies, 129, Transp Porous Media, 2019, pp. 501–520, https://doi.org/10.1007/s11242-018-1221-0.

[70] M.A. Perras, D. Vogler, Compressive and Tensile Behavior of 3D-Printed and Natural Sandstones, 129, Transp Porous Media, 2019, pp. 559–581, https://doi.org/10.1007/s11242-018-1153-8.

[71] L. Kong, M. Ostadhassan, B. Liu, M. Eshraghi, C. Li, M. Navarro, Y. Zhang, H. Wei, A comparison of three-dimensional–printed porous rocks with nano x-ray computed tomography: silica sand, gypsum powder, and resin, Am. Assoc. Petrol. Geol. Bull. 105 (2021) 2245–2261, https://doi.org/10.1306/08142019028.

[72] A. Suzuki, N. Watanabe, K. Li, R.N. Horne, Fracture network created by 3-D printer and its validation using CT images, Water Resour. Res. 53 (2017) 6330–6339, https://doi.org/10.1002/2017WR021032.

[73] D. Head, T. Vanorio, Effects of changes in rock microstructures on permeability: 3-D printing investigation, Geophys. Res. Lett. 43 (2016) 7494–7502, https://doi.org/10.1002/2016GL069334.

[74] S. Ishutov, F.J. Hasiuk, 3D printing berea sandstone: testing a new tool for petrophysical analysis of reservoirs, Petrophysics 58 (2017) 592–602.

[75] M.S. Jouini, J.S. Gomes, M. Tembely, E.R. Ibrahim, Upscaling strategy to simulate permeability in a carbonate sample using machine learning and 3D printing, IEEE Access 9 (2021) 90631–90641, https://doi.org/10.1109/ACCESS.2021.3091772.

[76] E.R. Ibrahim, M.S. Jouini, F. Bouchaala, J. Gomes, Simulation and validation of porosity and permeability of synthetic and real rock models using three-dimensional printing and digital rock physics, ACS Omega 6 (2021) 31775–31781, https://doi.org/10.1021/acsomega.1c04429.

[77] B. Li, J. Wang, R. Liu, Y. Jiang, Nonlinear fluid flow through three-dimensional rough fracture networks: insights from 3D-printing, CT-scanning, and high-resolution numerical simulations, J. Rock Mech. Geotech. Eng. 13 (2021) 1020–1032, https://doi.org/10.1016/j.jrmge.2021.04.007.

[78] R. Song, Y. Wang, S. Sun, J. Liu, Characterization and microfabrication of natural porous rocks: from micro-CT imaging and digital rock modelling to micro-3D-printed rock analogs, J. Pet. Sci. Eng. 205 (2021), 108827, https://doi.org/10.1016/j.petrol.2021.108827.

[79] F. Hasiuk, S. Ishutov, A. Pacyga, Validating 3D-printed porous proxies by tomography and porosimetry, Rapid Prototyp. J. 24 (2018) 630–636, https://doi.org/10.1108/RPJ-06-2017-0121.

[80] S. Ishutov, Establishing Framework for 3D Printing Porous Rock Models in Curable Resins, 129, Transp Porous Media, 2019, pp. 431–448, https://doi.org/10.1007/s11242-019-01297-9.

[81] J. Goral, M. Deo, Nanofabrication of synthetic nanoporous geomaterials: from nanoscale-resolution 3D imaging to nano-3D-printed digital (shale) rock, Sci. Rep. 10 (2020) 1–12, https://doi.org/10.1038/s41598-020-78467-z.

[82] A. Li, S. Zhang, C. Xu, X. Zhao, X. Zhang, 3D printing of true pore-scale berea sandstone and digital rock verification, SPE J. 26 (2021) 3719–3724, https://doi.org/10.2118/205383-PA.

[83] S. Ishutov, K. Hodder, R. Chalaturnyk, G. Zambrano_Narvaez, Replication of Carbonate Reservoir Pores at the Original Scale Using 3D Printing, Petrophysics 62 (2021) 477–485, https://doi.org/10.30632/PJV62N5-2021a3.

[84] L. Kong, Innovation of Petrophysical and Geomechanical Experiment Methodologies: the Application of 3D Printing Technology, University of North Dakota, 2019.

[85] S. Ishutov. 3D Printing Porous Proxies as a New Tool for Laboratory and Numerical Analyses of Sedimentary Rocks, Iowa State University, 2017.

[86] Z. Chen, Z. Li, J. Li, C. Liu, C. Lao, Y. Fu, C. Liu, Y. Li, P. Wang, Y. He, 3D printing of ceramics: a review, J. Eur. Ceram. Soc. 39 (2019) 661–687, https://doi.org/10.1016/j.jeurceramsoc.2018.11.013.

[87] I.L. de Camargo, M.M. Morais, C.A. Fortulan, M.C. Branciforti, A review on the rheological behavior and formulations of ceramic suspensions for vat photopolymerization, Ceram. Int. 47 (2021) 11906–11921, https://doi.org/10.1016/j.ceramint.2021.01.031.

[88] O. Santoliquido, P. Colombo, A. Ortona, Additive Manufacturing of ceramic components by Digital Light Processing: a comparison between the "bottom-up" and the "top-down" approaches, J. Eur. Ceram. Soc. 39 (2019) 2140–2148, https://doi.org/10.1016/j.jeurceramsoc.2019.01.044.

[89] Q. Lian, F. Yang, H. Xin, D. Li, Oxygen-controlled bottom-up mask-projection stereolithography for ceramic 3D printing, Ceram. Int. 43 (2017) 14956–14961, https://doi.org/10.1016/j.ceramint.2017.08.014.

[90] Z. Chen, X. Sun, Y. Shang, K. Xiong, Z. Xu, R. Guo, S. Cai, C. Zheng, Dense ceramics with complex shape fabricated by 3D printing: a review, J. Adv. Ceram. 10 (2021) 195–218, https://doi.org/10.1007/s40145-020-0444-z.

[91] A. Zocca, P. Colombo, C.M. Gomes, J. Günster, Additive manufacturing of ceramics: issues, potentialities, and opportunities, J. Am. Ceram. Soc. 98 (2015) 1983–2001, https://doi.org/10.1111/jace.13700.

[92] C. Paredes, F.J. Martínez-Vázquez, H. Elsayed, P. Colombo, A. Pajares, P. Miranda, Evaluation of direct light processing for the fabrication of bioactive ceramic scaffolds: effect of pore/strut size on manufacturability and mechanical performance, J. Eur. Ceram. Soc. 41 (2021) 892–900, https://doi.org/10.1016/j.jeurceramsoc.2020.09.002.

[93] D.M. Shah, J. Morris, T.A. Plaisted, A.V. Amirkhizi, C.J. Hansen, Highly filled resins for DLP-based printing of low density, high modulus materials, Addit. Manuf. 37 (2021), 101736, https://doi.org/10.1016/j.addma.2020.101736.

[94] H. Xing, B. Zou, Q. Lai, C. Huang, Q. Chen, X. Fu, Z. Shi, Preparation and characterization of UV curable Al2O3 suspensions applying for stereolithography 3D printing ceramic microcomponent, Powder Technol. 338 (2018) 153–161, https://doi.org/10.1016/j.powtec.2018.07.023.

[95] H. Xing, B. Zou, X. Liu, X. Wang, Q. Chen, X. Fu, Y. Li, Effect of particle size distribution on the preparation of ZTA ceramic paste applying for stereolithography 3D printing, Powder Technol. 359 (2020) 314–322, https://doi.org/10.1016/j.powtec.2019.09.066.

[96] M. Borlaf, N. Szubra, A. Serra-Capdevila, W.W. Kubiak, T. Graule, Fabrication of ZrO2 and ATZ materials via UV-LCM-DLP additive manufacturing technology, J. Eur. Ceram. Soc. 40 (2020) 1574–1581, https://doi.org/10.1016/j.jeurceramsoc.2019.11.037.

[97] M. Schwentenwein, J. Homa, Additive manufacturing of dense alumina ceramics, Int. J. Appl. Ceram. Technol. 12 (2015) 1–7, https://doi.org/10.1111/ijac.12319.

[98] M. Borlaf, A. Serra-Capdevila, C. Colominas, T. Graule, Development of UV-curable ZrO2 slurries for additive manufacturing (LCM-DLP) technology, J. Eur. Ceram. Soc. 39 (2019) 3797–3803, https://doi.org/10.1016/j.jeurceramsoc.2019.05.023.

[99] H. Xing, B. Zou, S. Li, X. Fu, Study on surface quality, precision and mechanical properties of 3D printed ZrO2 ceramic components by laser scanning stereolithography, Ceram. Int. 43 (2017) 16340–16347, https://doi.org/10.1016/j.ceramint.2017.09.007.

[100] I. Gibson, D. Rosen, B. Stucker, Additive Manufacturing Technologies: 3D Printing, Rapid Prototyping, and Direct Digital Manufacturing, second ed., second ed., Springer New York, New York, NY, 2015 https://doi.org/10.1007/978-1-4939-2113-3.

[101] M.L. Griffith, J.W. Halloran, Freeform fabrication of ceramics via stereolithography, J. Am. Ceram. Soc. 79 (1996) 2601–2608, https://doi.org/10.1111/j.1151-2916.1996.tb09022.x.

[102] I.L. de Camargo, C.A. Fortulan, H.A. Colorado, A review on the ceramic additive manufacturing technologies and availability of equipment and materials, Cerâmica 68 (2022) 329–347, https://doi.org/10.1590/0366-69132022683873331.

[103] S. Zakeri, M. Vippola, E. Levänen, A comprehensive review of the photopolymerization of ceramic resins used in stereolithography, Addit. Manuf. 35 (2020), 101177, https://doi.org/10.1016/j.addma.2020.101177.

[104] Y. Chen, N. Wang, O. Ola, Y. Xia, Y. Zhu, Porous ceramics: light in weight but heavy in energy and environment technologies, Mater. Sci. Eng. R. 143 (2021), 100589, https://doi.org/10.1016/j.mser.2020.100589.

[105] H. Shaked, I. Polishchuk, A. Nagel, Y. Bekenstein, B. Pokroy, Long-term stabilized amorphous calcium carbonate—an ink for bio-inspired 3D printing, Mater. Today Bio. 11 (2021), 100120, https://doi.org/10.1016/j.mtbio.2021.100120.

[106] M. Sauerwein, E.L. Doubrovski, Local and recyclable materials for additive manufacturing: 3D printing with mussel shells, Mater. Today Commun. 15 (2018) 214–217, https://doi.org/10.1016/j.mtcomm.2018.02.028.

[107] S.H. Ji, D.S. Kim, M.S. Park, J.S. Yun, Sintering process optimization for 3YSZ ceramic 3D-printed objects manufactured by stereolithography, Nanomaterials 11 (2021) 192, https://doi.org/10.3390/nano11010192.

[108] X. Li, H. Zhong, J. Zhang, Y. Duan, H. Bai, J. Li, D. Jiang, Dispersion and properties of zirconia suspensions for stereolithography, Int. J. Appl. Ceram. Technol. 17 (2020) 239–247, https://doi.org/10.1111/ijac.13321.

[109] I.L. de Camargo, R. Erbereli, H. Taylor, C.A. Fortulan, 3Y-TZP DLP additive manufacturing: solvent-free slurry development and characterization, Mater. Res. 24 (2021) 2–9, https://doi.org/10.1590/1980-5373-mr-2020-0457.

[110] I.L. de Camargo, R. Erbereli, C.A. Fortulan, Additive manufacturing of electrofused mullite slurry by digital light processing, J. Eur. Ceram. Soc. 41 (2021) 7182–7188, https://doi.org/10.1016/j.jeurceramsoc.2021.07.005.

[111] I.L. de Camargo, R. Erbereli, J.F.P. Lovo, R. Fortulan, C.A. Fortulan, Digital light processing additive manufacturing of in situ mullite-zirconia composites, J. Eur. Ceram. Soc. 42 (2022) 6025–6032, https://doi.org/10.1016/j.jeurceramsoc.2022.06.042.

[112] R. Erbereli, I.L. de Camargo, M.M. Morais, C.A. Fortulan, 3D printing of trabecular bone-mimetic structures by vat photopolymerization of bovine hydroxyapatite as a potential candidate for scaffolds, J. Braz. Soc. Mech. Sci. Eng. 44 (2022) 170, https://doi.org/10.1007/s40430-022-03468-0.

[113] C.W. Macosko, Rheology: Principles, Measurements and Applications, Wiley-VCH, New York, 1994.

[114] I.M. Krieger, T.J. Dougherty, A mechanism for non-Newtonian flow in suspensions of rigid spheres, Trans. Soc. Rheol. 3 (1959) 137–152, https://doi.org/10.1122/1.548848.
[115] M. Shen, W. Zhao, B. Xing, Y. Sing, S. Gao, C. Wang, Z. Zhao, Effects of exposure time and printing angle on the curing characteristics and flexural strength of ceramic samples fabricated via digital light processing, Ceram. Int. 46 (2020) 24379–24384, https://doi.org/10.1016/j.ceramint.2020.06.220.
[116] H. Wu, Y. Cheng, W. Liu, R. He, M. Zhou, S. Wu, X. Song, Y. Chen, Effect of the particle size and the debinding process on the density of alumina ceramics fabricated by 3D printing based on stereolithography, Ceram. Int. 42 (2016) 17290–17294, https://doi.org/10.1016/j.ceramint.2016.08.024.
[117] C.M. Barros Calado, M.S. Iturri, V.C. Colonetti, V. Constantino de Souza, C. P. Fernandes, D. Hotza, M.G. Novy Quadri, Green production of cellular ceramics by emulsification of sunflower oil followed by gelcasting and starch consolidation, J. Clean. Prod. 282 (2021), https://doi.org/10.1016/j.jclepro.2020.124468.
[118] X. Zhang, C. Bai, Y. Qiao, X. Wang, D. Jia, H. Li, P. Colombo, Porous geopolymer composites: a review, Compos. Part A Appl. Sci. Manuf. 150 (2021), https://doi.org/10.1016/j.compositesa.2021.106629.